Monthly Notices
of the
ROYAL ASTRONOMICAL SOCIETY

Mon. Not. R. Astron. Soc. **402,** 2441–2452 (2010) doi:10.1111/j.1365-2966.2009.16048.x

The quasar $\mathcal{M}_{\rm BH}$–$\mathcal{M}_{\rm host}$ relation through cosmic time – I. Data set and black hole masses

R. Decarli,[1⋆] R. Falomo,[2] A. Treves,[1] J. K. Kotilainen,[3] M. Labita[1] and R. Scarpa[4]

[1]*Università degli Studi dell'Insubria, via Valleggio 11, 22100 Como, Italy*
[2]*INAF – Osservatorio Astronomico di Padova, Vicolo dell'Osservatorio 5, 35122 Padova, Italy*
[3]*Tuorla Observatory, Department of Physics and Astronomy, University of Turku, Väisäläntie 20, FI–21500 Piikkiö, Finland*
[4]*Instituto de Astrofisica de Canarias, Via Lactea, s/n E38205 La Laguna, Tenerife, Spain*

Accepted 2009 November 10. Received 2009 October 27; in original form 2009 August 7

ABSTRACT

We study the $\mathcal{M}_{\rm BH}$–$\mathcal{M}_{\rm host}$ relation as a function of cosmic time in a sample of 96 quasars from $z = 3$ to the present epoch. In this paper, we describe the sample, the data sources and the new spectroscopic observations. We then illustrate how we derive $\mathcal{M}_{\rm BH}$ from single-epoch spectra, pointing out the uncertainties in the procedure. In a companion paper, we address the dependence of the ratio between the black hole mass and the host-galaxy luminosity and mass on cosmic time.

Key words: galaxies: active – galaxies: nuclei – quasars: emission lines – quasars: general.

1 INTRODUCTION

The discovery of tight relations between the mass of massive black holes (BHs), $\mathcal{M}_{\rm BH}$, and the large-scale properties of the galaxies where they reside (see Ferrarese 2006, for a review) is one of the most intriguing results in astrophysics of the last decade, given the consequences in the frame of galaxy formation and evolution. When and how these relations are set are still open questions.

Measuring $\mathcal{M}_{\rm BH}$ of quiescent massive BHs is extremely challenging even in nearby galaxies, and has been done successfully only in few tens of cases (Ferrarese 2006; Pastorini et al. 2007). By contrast, an estimate of $\mathcal{M}_{\rm BH}$ in type I active galactic nuclei (AGN) is possible by assuming that the gas emitting broad lines is in virial equilibrium (Peterson & Wandel 2000, but see also Marconi et al. 2008 and references therein for possible effects of non-virial components), and that the linewidth traces the BH potential well. Based on reverberation mapping studies (Blandford & McKee 1982), Kaspi et al. (2000) found a correlation between the characteristic size of the broad-line region (BLR) and the continuum luminosity of the AGN. This allows an estimate of the BH mass from single-epoch low-resolution spectra.

In order to sample the BH–host-galaxy relations through a wide range of cosmic ages, one has to focus on the brightest AGN. Quasars have been detected up to $z \gtrsim 6$ (Fan et al. 2004). Large-field surveys, such as the Sloan Digital Sky Survey (SDSS), allowed a detailed spectroscopic study of ∼60 000 quasars with $z < 4$ (Shen et al. 2008, hereafter S08). The drawback is that the typical nuclear-to-host luminosity ratio in quasars is such that the light from the host galaxy is outshone by the nuclear component. This usually prevents the detection of stellar features in the spectra of bright quasars. Only through the excellent resolution of the *Hubble Space Telescope* (*HST*), together with state-of-art observing techniques in the near-infrared (NIR) at ground-based telescopes, the detection of the extended emission of the host galaxies of few hundreds of quasars up to $z \lesssim 3$ became possible (see Kotilainen et al. 2009, and references therein).

In this project, we focus on quasars in the redshift range $0 < z < 3$ with known host-galaxy luminosity, in order to study the evolution of the $\mathcal{M}_{\rm BH}$–$\mathcal{M}_{\rm host}$ relation. This will shed some light on the joint evolution of BHs and galaxies up to and immediately beyond the crucial age of maximum quasar activity (Dunlop & Peacock 1990) and star formation (Madau, Pozzetti & Dickinson 1998). Here, we present the sample, the new spectroscopic observations, and we infer the BH masses. In a companion paper (Decarli et al. 2009c, hereafter Paper II), we address the topic of the $\mathcal{M}_{\rm BH}$–$\mathcal{M}_{\rm host}$ relation as a function of cosmic time.

Throughout this paper, we adopt a concordance cosmology with $H_0 = 70\,{\rm km\,s^{-1}\,Mpc^{-1}}$, $\Omega_{\rm m} = 0.3$, $\Omega_\Lambda = 0.7$. We converted the results of other authors to this cosmology when adopting their relations and data.

2 THE SAMPLE

Up to now, few hundreds of quasar host galaxies have been resolved at $z < 3$. In order to minimize the uncertainties due to colour and filter corrections, we select objects observed with filters roughly sampling the rest-frame *R* band. Furthermore, as the $\mathcal{M}_{\rm BH}$–$\mathcal{M}_{\rm host}$ relation is sensitive to the spheroidal rather than the total mass of the host galaxy (Marconi & Hunt 2003; Häring & Rix 2004), we consider only those targets with host galaxies classified as elliptical. Our sample consists of the following.

⋆E-mail: roberto.decarli@mib.infn.it

(i) 43 low-redshift ($z \lesssim 0.5$) quasars imaged with the *HST* wide-field camera (Bahcall et al. 1997; Hooper, Impey & Foltz 1997; Boyce et al. 1998; Kirhakos et al. 1999; Hamilton, Casertano & Turnshek 2002; Dunlop et al. 2003; Pagani, Falomo & Treves 2003; Floyd et al. 2004; Labita et al. 2006, hereafter L06; Kim et al. 2008). They represent the bulk of our knowledge of low-z quasar host galaxies. UV spectra of 28 of these quasars are taken from the *HST* Faint Object Spectrograph archive (see L06). For 36 objects, we collect optical spectra from the SDSS (Adelman-McCarthy et al. 2007, 13 quasars) and through on-purpose observations taken at the Asiago Telescope (23 quasars; see Decarli et al. 2008, hereafter D08).

(ii) 60 mid- and high-redshift ($z > 0.5$) quasars imaged in the NIR through ground-based observations under optimal seeing conditions performed by our group (50 objects; see Kotilainen, Falomo & Scarpa 1998; Kotilainen & Falomo 2000; Falomo et al. 2004, 2005; Hyvönen et al. 2007a,b; Kotilainen et al. 2007; Falomo et al. 2008; Decarli, Treves & Falomo 2009a; Kotilainen et al. 2009) or from *HST*-based compilations (10 sources from Kukula et al. 2001; Ridgway et al. 2001). We note that all these studies have very high host-galaxy detection rates (>85 per cent at $z < 2$, >60 per cent beyond $z = 2$). Optical spectra were collected at the Nordic Optical Telescope (NOT) and the European Southern Observatory (ESO)/3.6-m telescope (see Section 3).

The five unresolved quasars in Kotilainen et al. (2009) were spectroscopically observed when the analysis of the imaging data had not yet been completed. They are not included in the study of the evolution of the $\mathcal{M}_{\rm BH}$–$\mathcal{M}_{\rm host}$ relation. Other two objects were dropped, as we could not estimate $\mathcal{M}_{\rm BH}$ from our spectra (see Appendix A). Therefore, the final sample consists of 96 quasars. According to the Veron-Cetty & Veron (2006) catalogue, 48 of them are radio-loud quasars (RLQs) and 48 are radio-quiet quasars (RQQs). We remark that our sample is approximately twice as large as those of Peng et al. (2006a,b) and McLure et al. (2006) and represents the largest data set ever considered in the study of the evolution of the $\mathcal{M}_{\rm BH}$–$\mathcal{M}_{\rm host}$ relation. The distribution of our targets in the (z, M_V) plane is shown in Fig. 1. Table A1 lists the main properties of each quasar in our sample.

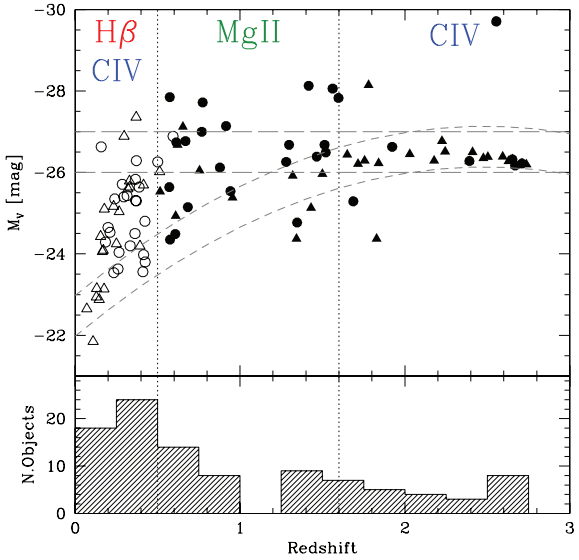

Figure 1. The distribution of the quasars in our sample in the (z, M_V) plane. M_V is the total rest-frame V-band absolute magnitude of the quasars, estimated from the V-band apparent magnitudes available in the Veron-Cetty & Veron (2006) catalogue and k-corrected assuming the quasar template by Francis et al. (1991). Filled symbols refer to the mid- and high-z data for which we present optical spectroscopy in this paper. Empty symbols mark the $z \lesssim 0.5$ data from L06 and D08. Circles and triangles represent RLQ and RQQ, respectively. The broad emission lines observed in the various redshift windows are also labelled. We note that the $-27 < M_V < -26$ luminosity range (long- dashed lines) as well as the $M_*(z) > M_V > M_*(z) - 1$ [where $M_*(z)$ is the characteristic luminosity of the quasar luminosity function by Boyle et al. (2000), plotted in short-dashed lines] are well sampled at any redshift bin.

Table 1. List of the observing runs.

Run (1)	Telescope (2)	Nights (3)	No. obj. (4)
E77	ESO/3.6 m	2005 September 30–October 1	6
E78	ESO/3.6 m	2007 March 23–25	12
E79	ESO/3.6 m	2007 September 8–12	22
N35	NOT	2007 April 9–10	2
N36	NOT	2007 October 17–19	18

Note. (1) Run ID. (2) Telescope (3) Dates of observations. (4) Number of observed objects per run.

3 NEW OBSERVATIONS, DATA REDUCTION

Spectra of the $z > 0.5$ quasars were collected in five observing runs at the ESO/3.6-m telescope in La Silla (Chile) and at the 2.56 m NOT in La Palma (Spain). Table 1 lists the dates of the observations and the number of spectra collected in each run, while Table A2 summarizes the journal of observations.

The ESO Faint Object Spectrograph and Camera (v.2, EFOSC2; see Buzzoni et al. 1984) and its twin NOT instrument, the Andalucia Faint Object Spectrograph and Camera (ALFOSC), were mounted in long-slit spectroscopy configuration. EFOSC2 observations were carried out with grism 4, yielding a spectral resolution of $R \sim 400$ (1.2 arcsec slit) in the spectral range 4100–7500 Å ($\Delta\lambda$/pixel = 3.36 Å pixel^{-1}). For NOT observations, we used ALFOSC grisms 6 and 7, which allow the observation of the 3500–5530[1] and 3800–6840 Å windows with spectral resolutions $R \sim 490$ and 650 with the 1.0 arcsec slit ($\Delta\lambda$/pixel $\approx$ 1.5 Å pixel^{-1}). At the central wavelength, the instrumental resolutions are 12.6 Å (EFOSC2+grism 4) and 8.2 Å (ALFOSC+grism 6 and 7).

Standard IRAF tools were used in the data reduction. The CCDRED package was employed to perform bias subtraction, flat field correction, image alignment and combination. Cosmic rays were eliminated by combining three or more exposures of the same objects, and applying CRREJECT algorithm while averaging. When only one or two bidimensional spectra were available, we applied the COSMICRAYS task in the CRUTILS package. In these cases, in order to prevent the task from altering the narrow component of emission lines, we masked the central region of our bidimensional spectra. The spectra extraction, the background subtraction and the calibrations both in wavelength and in flux were performed with DOSLIT task in SPECRED package, using He–Ar, Th–Ar and He–Ne lamps and spectrophotometric standard stars as references. Wavelength calibration residuals are around 0.5, 0.35 and 0.03 Å in the three adopted setups (subpixel), thus implying a negligible (<1 per cent) error on redshift

[1]The nominal observed range of ALFOSC grism 6 is larger bluewards, but the sensitivity is so low that we decided to drop the observed spectra at wavelengths below 3500 Å.

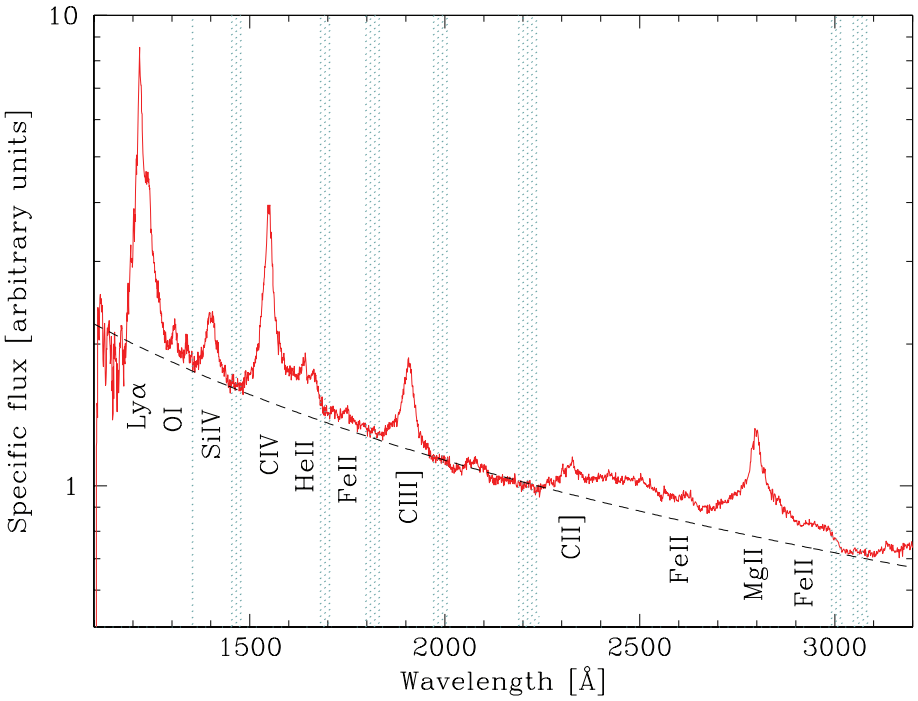

Figure 2. The combined spectrum of the quasars considered in the present study, normalized to the continuum value at 2250 Å. The median spectrum is plotted with a solid line. Main emission lines are labelled. The shaded regions mark the intervals used in the fit of the continuum. The resulting fit is plotted as a dashed line.

estimates. Absolute flux calibration of spectra was corrected through the photometry of field stars, as described in D08. This procedure yields uncertainties in the flux calibration as low as 0.05 mag (see, e.g. Kotilainen et al. 2009), and commonly around 0.1 mag. Photometric accuracy of each target is reported in Table A2. Galactic extinction was accounted for according to Schlegel, Finkbeiner & Davis (1998), assuming $R_V = 3.1$. We shifted the spectra to the rest frame, according to the catalogue z, remembering that quasar lines with different ionization potentials may present slightly different shifts (e.g. Bonning, Shields & Salviander 2007). Average signal-to-noise ratio (S/N) of our spectra is ∼30. The composite spectrum, obtained by median averaging rest-frame individual observations of these new data, is presented in Fig. 2. The whole data set is available electronically at www.dfm.uninsubria.it/astro/caqos/.

4 DATA ANALYSIS

We focus our attention on the analysis required to estimate $\mathcal{M}_{\rm BH}$ from single-epoch observations of the rest-frame UV spectra of quasars. Applied to the gas in the BLR of type 1 AGN, the virial paradigm yields

$$\mathcal{M}_{\rm BH} = G^{-1} R_{\rm BLR} v_{\rm BLR}^2, \quad (1)$$

where $R_{\rm BLR}$ is the characteristic radius of the broad-line emission, and $v_{\rm BLR}$ is the velocity of the emitting clouds at $R_{\rm BLR}$.

The cloud velocity can be inferred from the width of the broad emission lines, e.g.

$$v_{\rm BLR} = f \times {\rm FWHM}, \quad (2)$$

where f is a geometrical factor around unity which accounts for the deprojection of $v_{\rm BLR}$ from the line of sight, and FWHM is the full width at half maximum of the line profile (see McGill et al. 2008 and D08 for discussions on other linewidth parametrizations).

On the other hand, the BLR size cannot be directly measured from single-epoch spectra. Our estimates of the BLR size rely on the discovery that $R_{\rm BLR}$ scales with a certain power of the continuum luminosity of the AGN, λL_λ (see Kaspi et al. 2000), as expected from simple photoionization models.

4.1 The continuum luminosity and the BLR size

Quasar UV–optical spectra are characterized by the superposition of the following components:

(1) a power-law-like continuum from the nucleus;
(2) broad lines emitted within the BH influence radius;
(3) narrow emission lines from the quasar host galaxy and the AGN narrow-line region;
(4) the star light continuum from the host galaxy;
(5) a pseudo-continuum due to the blending of several Fe II and Fe III multiplets.

In order to infer the BLR radius, we have to isolate the first component from the others. Our spectra cover the rest-frame UV range of bright AGN, where the flux from the host-galaxy star light is always negligible. The contamination of both broad and narrow emission lines is usually avoided simply by fitting the power-law continuum to the observed spectra in a number of wavelength windows free of strong features. Here, we adopted the intervals: 1351–1362, 1452–1480, 1680–1710, 1796–1834, 1970–2010, 2188–2243, 2950–2990 and 3046–3090 Å (see Fig. 2). The fitted parameters, together with the derived monochromatic specific fluxes and luminosities are reported in Table A3. We note that the luminosity estimates obtained through the fit of the power-law component and those obtained from a direct measure of the continuum at 1350 and 3000 Å are practically equivalent in our data sets, the differences being <10 per cent on average.

Concerning luminosity–radius relations, simple photoionization models with a constant ionization parameter predict that an ionizing source emitting isotropically affects a region with a characteristic radius scaling as the square root of the source luminosity. This dependence has been confirmed in several reverberation mapping studies focused on Hβ. Time-lag data of the rest-frame UV lines are still limited in number; therefore, any available relation for Mg II and C IV is affected by poor statistics (e.g. see fig. 6 in Kaspi et al. 2007). For consistency with our low-redshift studies, we will refer to the relations provided by McLure & Jarvis (2002) for Mg II:[2]

$$\frac{R_{\rm BLR}({\rm Mg\,II})}{10\ {\rm light\text{-}days}} = (2.52 \pm 0.3) \left[\frac{\lambda L_\lambda (3000\ {\rm \AA})}{10^{44}\ {\rm erg\ s^{-1}}}\right]^{0.47\pm0.05} \quad (3)$$

and by Kaspi et al. (2007) for C IV:

$$\frac{R_{\rm BLR}({\rm C\,IV})}{10\ {\rm light\text{-}days}} = (0.24 \pm 0.06) \left[\frac{\lambda L_\lambda (1350\ {\rm \AA})}{10^{43}\ {\rm erg\ s^{-1}}}\right]^{0.55\pm0.04} . \quad (4)$$

All these relations are based on low-redshift ($z < 0.3$) objects, with the only exception of S5 0836+71 ($z = 2.17$; see Kaspi et al. 2007). Throughout this work, we assume that no significant cosmic evolution of the radius–luminosity relations occurs in the sampled redshift range.

The C IV relation is poorly constrained, as mentioned above, especially in the bright side where most of our objects reside. Assuming a different slope of the luminosity–time-lag relation, e.g. 0.5, affects our radius estimates at $\lambda L_\lambda \sim 10^{47}$ erg s^{-1} up to 0.2 dex (i.e. a factor of $\approx$1.7). Nevertheless, we stress here that in terms of $\mathcal{M}_{\rm BH}$ estimates such a difference would result in a global offset of all values and in a redefinition of the geometrical factor f, with little effect on the evolution of the $\mathcal{M}_{\rm BH}$–$\mathcal{M}_{\rm host}$ relation.

The scatter around the luminosity–radius relations dominates the uncertainties in the radius estimates, contributing up to a factor of $\sim$2, while the uncertainties in the luminosity estimates never exceed 10 per cent.

4.2 Emission linewidths and cloud velocities

Measuring the width of broad lines consists of three key steps: the definition of the local continuum, the removal of contaminating spectral features (in particular the Fe II multiplets) and the fit with a certain analytical function.

We define underlying continua by matching the fluxes in the windows 2230–2250 and 3020–3050 Å for Mg II and 1465–1485 and 1685–1705 Å for C IV, where no significant feature is observed (see Fig. 3). To evaluate the effects of Fe II contamination, we first fitted the Mg II and C IV lines in the 2720–2880 and 1490–1570 Å windows, where the Fe II contribution is less relevant. Then, we compared these estimates of the linewidths with those obtained by fitting the 2450–3020 and 1490–1620 Å regions with a superposition of a broad-line model plus a template reproducing the Fe II emission (Vestergaard & Wilkes 2001). In the latter approach, the Fe II emission observed in narrow-line type 1 AGN (usually IZw001) is taken as representative for all quasars, after being properly broadened. The validity of this assumption has been widely discussed in the literature, both from a theoretical and an observational point of view (e.g. Phillips 1978; Boroson & Green 1992; Marziani et al. 2003; Tsuzuki et al. 2006; McGill et al. 2008). Since most Fe II lines are blended with each other, their width is hardly constrained. We therefore fixed their broadening to the width of C IV and Mg II lines. Fig. 3 shows examples of fits on C IV and Mg II. Linewidth estimates obtained with or without the Fe II modelling are usually consistent within 20 per cent, but Mg II shows few deviations larger than 30 per cent, especially when the Fe II emission is strong with respect to the line flux. Hereafter, we will refer to the line models obtained by template fitting the Fe II emission.

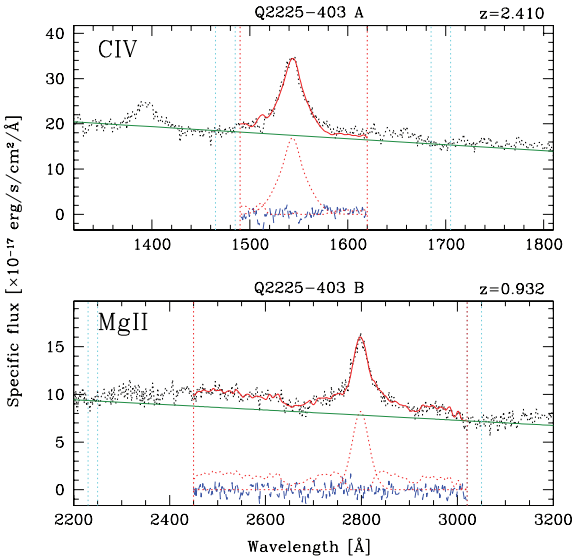

Figure 3. Examples of the line fit, for C IV in quasar Q2225−403 A (upper panel) and for Mg II in quasar Q2225−403 B (lower panel). The rest-frame observed spectra of the two quasars are shown by dotted lines. Dotted vertical lines mark the regions used for the underlying continuum estimates and the fitted wavelength range. The thin, solid lines show the continua underlying broad emission lines. The bold, solid lines are the broad-emission-line fits. In the bottom side of each panel, we plot the fitted Fe II template and the broad-line model (dotted lines) together with the fit residual (dashed line).

Concerning the fitted function, a single Gaussian usually does not provide satisfactory fits, especially for C IV (see D08; S08; Bon et al. 2009). We performed our analysis both with the sum of two Gaussian profiles with the same peak (hereafter G2) and the Gauss–Hermite series (GH; Van Der Marel & Franx 1993), truncated at the fourth order. Reduced χ^2 values obtained from these functions are similarly good, suggesting that both functions can describe line profiles reasonably well. No significant offset is observed among the linewidth estimates based on the two functions, the residuals lying within 20 per cent (see also fig. A1 in D08). We thus conclude that the two functions are equivalent to our purposes. We note that, since G2 fits are necessarily symmetric, while GH fits are not, the consistency between the two estimates of the linewidthsuggests that the FWHM is poorly sensitive to line-profile asymmetries. Throughout this paper, we will refer to the FWHM estimates based on GH fits.

[2]McLure & Jarvis (2002) set their relation by comparing the Hβ time lags to the continuum luminosity around 3000 Å, given the fact that Mg II and Hβ have similar ionizing potentials; hence, they are emitted in the same region. This assumption allows us to adopt the same geometrical factor for the Mg II BLR as the one derived in D08 for Hβ. Note that McLure & Jarvis (2002) fitted the line profile of Mg II into a broad and a narrow component and used only the former to infer $\mathcal{M}_{\rm BH}$ (although there is no evidence of significant narrow components in Mg II lines: see e.g. S08). As a consequence, the values of $\mathcal{M}_{\rm BH}$ reported in their study are systematically larger than ours, but our conclusions are unchanged as we adopt our own internal calibration of f.

Summarizing, we estimate that the typical uncertainties in the linewidth estimates due to the adopted fit procedures lie within 20 per cent, and usually even lower (if some modelling of the Fe II emission is adopted). Reduced χ^2 maps suggest that, given the high S/N of our data (exceeding 20 in all but few cases), formal uncertainties in the parameter estimates contribute to $\lesssim 10$ per cent of the FWHM value. Therefore, we conclude that typical uncertainties in the FWHM estimates are around 20 per cent.

5 VIRIAL ESTIMATES OF BH MASSES

In this section, we match the new estimates of the continuum luminosity, FWHM and $\mathcal{M}_{\rm BH}$ with those from our previous low-z studies (L06; D08).

In Fig. 4, we plot the distribution of our data in the (λL_λ, FWHM) plane (see a similar approach in Fine et al. 2008; Labita et al. 2009a). This allows us to monitor how observable quantities (here, the continuum luminosity of the quasar and the linewidths) affect our estimates of $\mathcal{M}_{\rm BH}$ and the Eddington ratio, $L/L_{\rm Edd}$, derived *assuming* equation (1), $f(\rm H\beta, Mg\,II) = 1.6$, $f(\rm C\,IV) = 2.4$ (as defined in equation 2 and in D08) and the bolometric corrections given in Richards et al. (2006): $L_{\rm bol}/\lambda L_\lambda = 9.26$, 5.15 and 3.81 for H$\beta$, Mg II and C IV, respectively. Average and rms values of FWHM, λL_λ, $\mathcal{M}_{\rm BH}$ and $L/L_{\rm Edd}$ are provided in Table 2, while data of individual quasars are given in Table A3.

Table 2. Average and rms values of FWHM (2), λL_λ (3), $\mathcal{M}_{\rm BH}$ (4) and $L/L_{\rm Edd}$ (5) for all the subsamples in this study.

Line	⟨log FWHM⟩ (km s^{-1})	⟨log λL_λ⟩ (erg s^{-1})	⟨log $\mathcal{M}_{\rm BH}$⟩ ($M_\odot$)	⟨log $L/L_{\rm Edd}$⟩
(1)	(2)	(3)	(4)	(5)
Low z				
Hβ	3.66 ± 0.19	45.01 ± 0.51	9.01 ± 0.47	-1.13 ± 0.45
C IV	3.60 ± 0.11	45.55 ± 0.56	9.06 ± 0.38	-1.03 ± 0.34
High z				
Mg II	3.63 ± 0.19	45.78 ± 0.54	9.21 ± 0.49	-0.82 ± 0.46
C IV	3.66 ± 0.19	45.74 ± 0.36	9.28 ± 0.47	-1.06 ± 0.41

The monochromatic luminosity at 5100 Å is on average 3.5 times fainter than at 1350 Å in the same redshift bin. This is consistent with an average power-law index of the quasar continuum α close to 2 (defined so that $F_\lambda \propto \lambda^{-\alpha}$). The 3000 Å luminosities sampled in our study range from few times 10^{44} to 10^{47}erg s^{-1}, the bulk being around 10^{46} erg s^{-1}. The C IV data at high z are more clustered

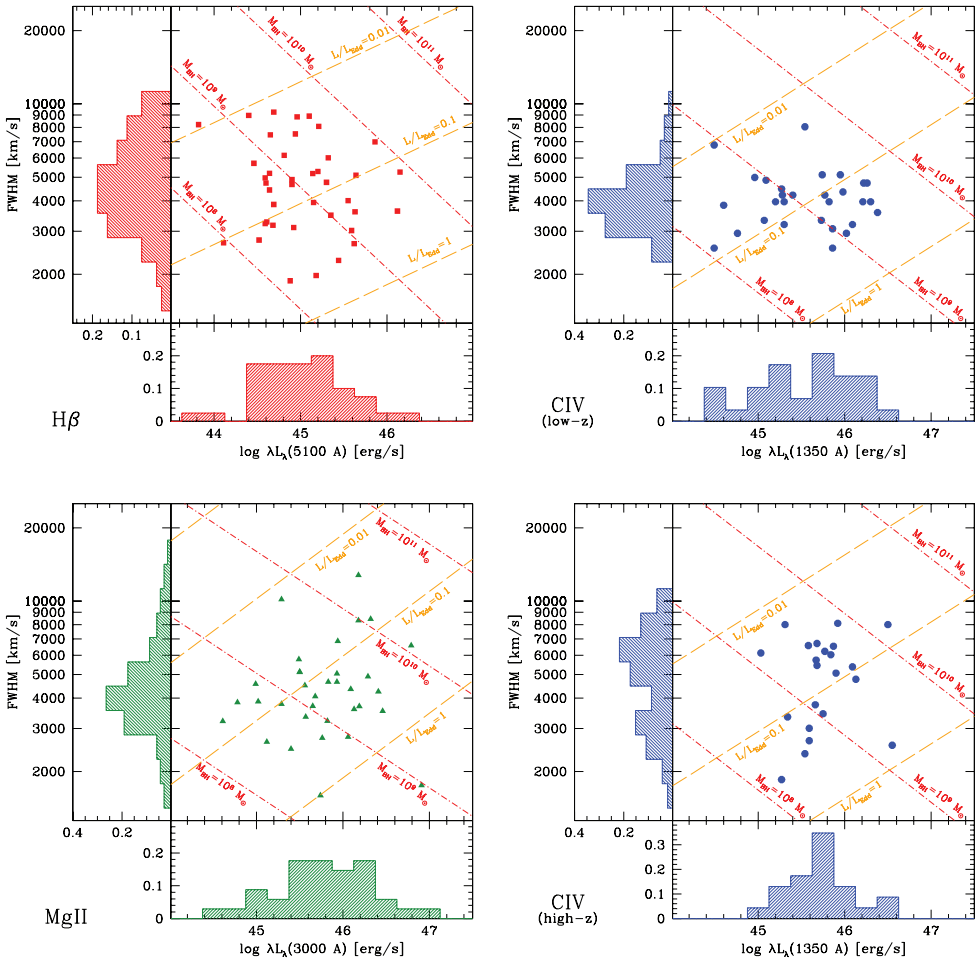

Figure 4. The distribution of our data in the (λL_λ, FWHM) plane, for Hβ, C IV at low z (upper panels), Mg II and C IV at high z (bottom panels). The (normalized) projections along each axis are also shown. The loci with constant $\mathcal{M}_{\rm BH}$ (dot–dashed lines) and $L/L_{\rm Edd}$ (dashed lines) are plotted. The values of Hβ FWHM show a wider distribution with respect to Mg II. Data are log-normally distributed both in the λL_λ and in the FWHM values. C IV data show less spread in the sampled λL_λ space and a flatter distribution in the linewidth with respect to the Mg II.

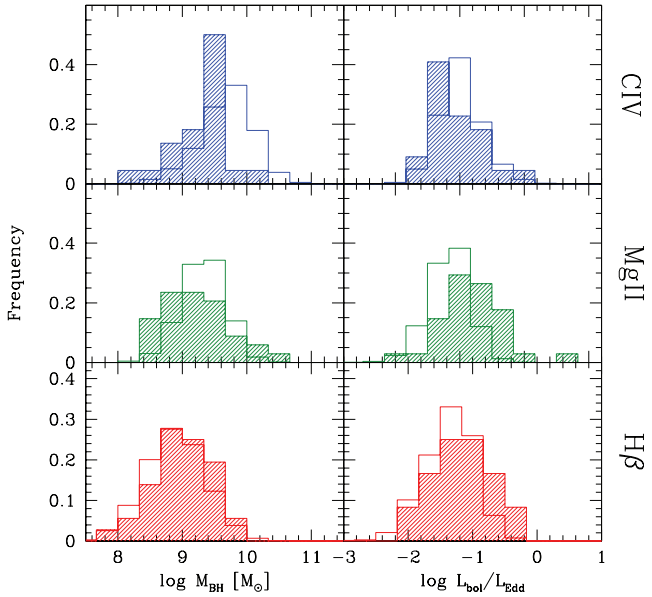

Figure 5. The distributions of $\mathcal{M}_{\rm BH}$ and $L/L_{\rm Edd}$ as derived from C IV (upper panels), Mg II (central panels) and Hβ (bottom panels). Low-z C IV-based estimates are not included, as no counterpart is available in the S08 sample. Shaded histograms refer to our objects, while empty histograms refer to the data set of S08.

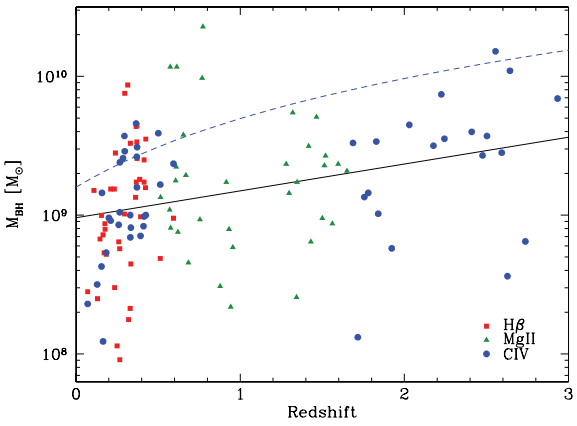

Figure 6. The redshift dependence of $\mathcal{M}_{\rm BH}$ for the quasars in our sample. Circles, triangles and squares refer to C IV, Mg II and Hβ-based $\mathcal{M}_{\rm BH}$ estimates. The best linear fit is shown as a solid line. The dashed line refers to the redshift evolution of the maximum $\mathcal{M}_{\rm BH}$ as derived by Labita et al. (2009b).

around approximately the same luminosity as Mg II data, $\approx 6 \times 10^{45}$ erg s^{-1}. This thinner distribution is due to the combination of two selection effects: lowest luminosity quasars are missed due to the Malmquist bias (the C IV line falls in the optical bands at $z > 1.6$, see Fig. 1); highest luminosity quasars were rejected in the studies of the host-galaxy luminosities, in order to make the detection of the extended emission around the nuclear source more feasible (see Fig. 1 and Kotilainen et al. 2009).

Concerning the linewidths, Hβ values show a wider dispersion with respect to the Mg II line, notwithstanding the two lines have similar ionization potential, thus they are believed to originate in the same regions (see also S08; Labita et al. 2009a,b). Low-redshift data from the C IV line show a smaller average value with respect to both Hβ and high-z C IV data, and a significantly narrower distribution (see the discussion in D08).

With only few exceptions, all our data reside in the locus defined by $10^8 \gtrsim \mathcal{M}_{\rm BH}/{\rm M}_\odot \gtrsim 10^{10}$ and $0.01 \gtrsim L/L_{\rm Edd} \gtrsim 1$.

In Fig. 5, we compare the distributions of $\mathcal{M}_{\rm BH}$ and $L/L_{\rm Edd}$ from our data set with the huge quasar sample from S08.[3] We dropped our low z, C IV-based data from this comparison as they do not have any counterpart in the S08 data. The distributions of BH masses and Eddington ratios computed from Hβ in our study are in substantial agreement with those by S08. On the other hand, the BH masses in our sample have increasingly smaller values than those from S08. We interpret this trend as the superposition of a number of effects: the luminosity cut adopted by Kotilainen et al. (2009) for $z > 2$ objects, the evolution of the luminosity and mass functions of active BHs through redshift and the occurrence of the Malmquist bias (on this topic; see Labita et al. 2009a,b). On average, the Eddington ratios sampled in our study do not show significant differences with respect to those in S08, nor evolution from $z = 0$ to 3.

The relatively small statistics and the luminosity-based selection of the targets in our sample hinder the study of the dependence of $\mathcal{M}_{\rm BH}$ on the redshift. We note that, on average, the higher is the redshift, the more massive are the BHs (see Fig. 6). The linear best fit is

$$\log \mathcal{M}_{\rm BH}/{\rm M}_\odot = (0.19 \pm 0.06)z + (8.98 \pm 0.06). \quad (5)$$

This trend is in qualitative agreement with the one found by Labita et al. (2009b) with a procedure aimed to minimize the Malmquist bias. However, the occurrence of selection biases cannot be ruled out in the present work.

6 CONCLUSIONS

We start from a list of 96 quasars with known host-galaxy luminosity. New, high-quality (S/N $\sim$ 30) spectra of the mid- and high-redshift targets ($z > 0.5$) are presented here and matched with those of low-z quasars we collected in our previous studies. We analyse the continuum luminosity and profiles of broad emission lines in order to infer BH masses. In particular, the C IV line is studied both at low and high redshifts, thus avoiding a systematic error related to the adopted emission line in the estimate of $\mathcal{M}_{\rm BH}$. We found that high-redshift quasars in our sample do have, on average, larger BH masses than local ones, but we note that this result is potentially affected by the luminosity selection and the Malmquist bias. In an accompanying Paper II, we study the ratio between $\mathcal{M}_{\rm BH}$ and the luminosity and mass of the host galaxies of the quasars in our sample, and its evolution as a function of the redshift.

ACKNOWLEDGMENTS

We thank the anonymous referee for his/her fruitful suggestions. This work was based on observations made with the NOT (programme ID: 35-039 and 36-039), operated on the island of La Palma jointly by Denmark, Finland, Iceland, Norway and Sweden, in the Spanish Observatorio del Roque de los Muchachos of the Instituto de Astrofisica de Canarias, and with the ESO/3.6-m telescope in La Silla [programme ID: 078.B-0087(A) and 079.B-0304(A)]. ALFOSC NOT is owned by the Instituto de Astrofisica de Andalucia (IAA) and operated at the NOT under agreement

[3] From S08 we take the values of z, FWHM and λL_λ of the objects in the same redshift ranges addressed in our study. All the derived quantities (e.g. $\mathcal{M}_{\rm BH}$ and $L/L_{\rm Edd}$) are recomputed following the recipes discussed in this work.

between IAA and the NBIfAFG of the Astronomical Observatory of Copenhagen.

This research has made use of the *VizieR Service*, available at http://vizier.u-strasbg.fr/viz-bin/VizieR and of the NASA/IPAC Extragalactic Database which is operated by the Jet Propulsion Laboratory, California Institute of Technology, under contract with the National Aeronautics and Space Administration. Observed spectra are available at www.dfm.uninsubria.it/astro/caqos/.

REFERENCES

Adelman-McCarthy J. K. et al., 2007, ApJS, 172, 634
Bahcall J. N., Kirhakos S., Saxe D. H., Schneider D. P., 1997, ApJ, 479, 642
Blandford R. D., McKee C. F., 1982, ApJ, 255, 419
Bon E., Popović L. Č., Gavrilović N., La Mura G., Mediavilla E., 2009, MNRAS, 400, 924
Bonning E. W., Shields G. A., Salviander S., ApJ, 666, L13
Boroson T. A., Green R. F., 1992, ApJS, 80, 109
Boyce P. J. et al., 1998, MNRAS, 298, 121
Boyle B. J., Shanks T., Croom S. M., Smith R. J., Miller L., Loaring N., Heymans C., 2000, MNRAS, 317, 1014
Buzzoni B. et al., 1984, ESO Messenger, 38, 9
Decarli R., Labita M., Treves A., Falomo R., 2008, MNRAS, 387, 1237 (D08)
Decarli R., Treves A., Falomo R., 2009a, MNRAS, 396, L31
Decarli R., Falomo R., Kotilainen J., Labita M., Scarpa R., Treves A., 2009b, Bentham Open Astron. J., 2
Decarli R., Falomo R., Treves A., Labita M., Kotilainen J. K., Scarpa R., 2009c, MNRAS, in press (doi:10.1111/j.1365-2966.2009.16049.x) (Paper II, this issue)
Drinkwater M. J., 1987, PhD thesis, Univ. Cambridge
Dunlop J. S., Peacock J. A., 1990, MNRAS, 247, 19
Dunlop J. S., McLure R. J., Kukula M. J., Baum S. A., O'Dea C. P., Hughes D. H., 2003, MNRAS, 340, 1095
Falomo R., Kotilainen J. K., Pagani C., Scarpa R., Treves A., 2004, ApJ, 604, 495
Falomo R., Kotilainen J. K., Scarpa R., Treves A., 2005, A&A, 434, 469
Falomo R., Treves A., Kotilainen J. K., Scarpa R., Uslenghi M., 2008, ApJ, 673, 694
Fan X. et al., 2004, AJ, 128, 515
Ferrarese L., 2006, in Colpi M., Gorini V., Haardt F., Moschella U., eds, Series in High Energy Physics, Cosmology and Gravitation, 'Joint Evolution of Black Holes and Galaxies'. Taylor & Francis Group, New York–London, p. 1
Fine S. et al., 2008, MNRAS, 390, 1413
Floyd D. J. E., Kukula M. J., Dunlop J. S., McLure R. J., Miller L., Percival W. J., Baum S. A., O'Dea C. P., 2004, MNRAS, 355, 196
Francis P. J., Hewett P. C., Foltz C. B., Chaffee F. H., Weymann R. J., Morris S. L., 1991, ApJ, 373, 465
Hamilton T. S., Casertano S., Turnshek D. A., 2002, ApJ, 576, 61
Häring N., Rix H.-W., 2004, ApJ, 604, L89
Hooper E. J., Impey C. D., Foltz C. B., 1997, ApJ, 480, L95
Hyvönen T., Kotilainen J. K., Orndhal E., Falomo R., 2007a, A&A, 462, 525
Hyvönen T., Kotilainen J. K., Falomo R., Orndhal E., Pursimo T., 2007b, A&A, 476, 723
Kaspi S., Smith P. S., Netzer H., Maoz D., Jannuzi B. T., Giveon U., 2000, ApJ, 533, 631
Kaspi S., Brandt W. N., Maoz D., Netzer H., Schneider D. P., Shemmer O., 2007, ApJ, 659, 997
Kim M., Ho L. C., Peng C. Y., Barth A. J., Im M., 2008, ApJS, 179, 283
Kirhakos S., Bahcall J. N., Schneider D. P., Kristian J., 1999, ApJ, 520, 67
Kotilainen J. K., Falomo R., 2000, A&A, 364, 70
Kotilainen J. K., Falomo R., Scarpa R., 1998, A&A, 332, 503
Kotilainen J. K., Falomo R., Labita M., Treves A., Uslenghi M., 2007, ApJ, 660, 1039
Kotilainen J. K., Falomo R., Decarli R., Treves A., Uslenghi M., Scarpa R., 2009, ApJ, 703, 1663
Kukula M. J., Dunlop J. S., McLure R. J., Miller L., Percival W. J., Baum S. A., O'Dea C. P., 2001, MNRAS, 326, 1533
Labita M., Treves A., Falomo R., Uslenghi M., 2006, MNRAS, 373, 551 (L06)
Labita M., Decarli R., Treves A., Falomo R., 2009a, MNRAS, 396, 1537
Labita M., Decarli R., Treves A., Falomo R., 2009b, MNRAS, 399, 2099
McGill K. L., Woo J. H., Treu T., Malkan M. A., 2008, ApJ, 673, 703
McLure R. J., Jarvis M. J., 2002, MNRAS, 337, 109
McLure R. J., Jarvis M. J., Targett T. A., Dunlop J. S., Best P. N., 2006, MNRAS, 368, 1395
Madau P., Pozzetti L., Dickinson M., 1998, ApJ, 498, 106
Marconi A., Hunt L. K., 2003, ApJ, 589, L21
Marconi A., Axon D. J., Maiolino R., Nagao T., Pastorini G., Pietrini P., Robinson A., Torricelli G., 2008, ApJ, 678, 693
Marziani P., Sulentic J. W., Zamanov R., Calvani M., Dultzin-Hacyan D., Bachev R., Zwitter T., 2003, ApJS, 145, 199
Pagani C., Falomo R., Treves A., 2003, ApJ, 596, 830
Pastorini G. et al., 2007, A&A, 469, 405
Peng C. Y., Impey C. D., Ho L. C., Barton E. J., Rix H.-W., 2006a, ApJ, 640, 114
Peng C. Y., Impey C. D., Rix H.-W., Kochanek C. S., Keeton C. R., Falco E. E., Lehár J., McLeod B. A., 2006b, ApJ, 649, 616
Peterson B. M., Wandel A., 2000, ApJ, 540, L13
Phillips M. M., 1978, ApJS, 38, 187
Richards G. T. et al., 2006, ApJS, 166, 470
Ridgway S., Heckman T., Calzetti D., Lehnert M., 2001, ApJ, 550, 122
Savage A., Trew A. S., Chen J.-S., Weston T., 1984, MNRAS, 207, 393
Schlegel D. J., Finkbeiner D. P., Davis M., 1998, ApJ, 500, 525
Schmidt M., 1977, ApJ, 217, 358
Shen Y., Greene J. E., Strauss M. A., Richards G. T., Schneider D. P., 2008, ApJ, 680, 169 (S08)
Tsuzuki Y., Kawara K., Yoshii Y., Oyabu S., Tanabe T., Matsuoka Y., 2006, ApJ, 650, 57
Van Der Marel R. P., Franx M., 1993, ApJ, 407, 525
Veron-Cetty M. P., Veron P., 2006, A&A, 455, 773
Vestergaard M., Wilkes B. J., 2001, ApJS, 134, 1
Zhan Y., Chen J.-S., 1989, Chinese Astron. Astrophys., 13, 139

APPENDIX A: NOTES ON INDIVIDUAL TARGETS

The catalogue by Veron-Cetty & Veron (2006) reports tentative redshifts for quasars 0119−370 ($z = 1.32$; Savage et al. 1984) and 0152−4055 ($z = 1.65$; Drinkwater 1987). Our spectra confirm both of them: from the peak wavelength of the Mg II line, we infer $z = 1.369$ for 0119−370 and $z = 1.632$ for 0152−4055.

PKS 0440−00 has a literature redshift of 0.844, inferred from the detection of a possible emission line at 5158 Å (Schmidt 1977). Our spectrum clearly shows that the Mg II line is actually present, but it is peaked at 4496 Å, yielding $z = 0.607$. The Fe II features around Mg II support the line identification. In particular, we note that a bump typical of the Fe II system redwards the Mg II line is observed at ∼5150 Å.

ZC2351+010B was classified as a quasar in objective prism survey by Zhan & Chen (1989), with a tentative redshift $z = 0.810$. Our spectrum shows the typical features of an M-type star (see a similar case in Decarli et al. 2009b).

Quasars 4C02.54 and PKS 1102−242 were observed during N36 and E78, respectively. Since the broad lines of interest fall right on the edges of the observed ranges of the collected spectra, we cannot infer reliable estimates of $\mathcal{M}_{BH}$ for these objects.

Table A1. The observed sample. All catalogue values are referred to Veron-Cetty & Veron (2006).

Name	RA (J2000)	Dec. (J2000)	z	Radio loudness	m_V (mag)	A_V (mag)	M_V (mag)	References
(1)	(2)	(3)	(4)	(5)	(6)	(7)	(8)	(9)
PKS 0000−177	00:03:22.0	−17:27:12	1.465	L	19.00	0.086	−26.39	E77
Q0040−3731	00:42:57.4	−37:15:31	1.780	Q	17.80	0.053	−28.15	E77
SGP2:36	00:51:14.3	−29:05:20	1.756	Q	19.62	0.046	−26.29	E79
SGP5:46	00:52:22.8	−27:30:03	0.955	Q	18.88	0.048	−25.38	E79
0054+144	00:57:09.9	+14:46:10	0.171	Q	15.70	0.151	−24.09	D08
SGP4:39	00:59:08.9	−27:51:25	1.716	Q	19.64	0.074	−26.21	E79
PKS 0100−270	01:02:56.3	−26:46:36	1.597	L	17.80	0.051	−27.83	E77
LBQS0100+0205	01:03:13.0	+02:21:10	0.393	Q	17.51	0.069	−24.19	L06
0110+297	01:13:24.2	+29:58:15	0.363	L	17.00	0.209	−24.50	D08
PKS 0113−283	01:15:23.9	−28:04:55	2.555	L	17.10	0.051	−29.71	E79
0119−370	01:21:24.1	−36:50:02	1.320	Q	19.20	0.058	−25.92	E79
0133+207	01:36:24.4	+20:57:27	0.425	L	18.10	0.203	−23.80	L06, D08
3C48	01:37:41.3	+33:09:35	0.367	L	16.20	0.144	−25.31	L06, D08
HB890137+012	01:39:57.2	+01:31:46	0.260	L	17.10	0.096	−23.63	L06
0152−4055	01:54:20.1	−40:40:30	1.650	Q	19.30	0.055	−26.44	E79
PKS 0155−495	01:57:38.0	−49:15:19	1.298	L	18.40	0.053	−26.68	E77
PKS 0159−11	02:01:57.1	−11:32:34	0.669	L	16.40	0.073	−26.77	N36
B0204+2916	02:07:02.2	+29:30:46	0.109	Q	16.80	0.212	−21.85	D08
0244+194	02:47:40.8	+19:40:58	0.176	Q	16.66	0.368	−23.14	D08
KUV03086−0447	03:11:04.7	−04:35:41	0.755	Q	17.50	0.284	−26.05	N36
MZZ01558	03:14:51.5	−54:57:14	1.829	Q	21.64	0.054	−24.37	E79
US3828	03:18:25.6	+15:59:56	0.515	Q	16.90	0.395	−25.53	N36
Q0335−3546	03:37:02.4	−35:36:39	1.841	Q	19.80	0.043	−26.23	E79
PKS 0348−120	03:51:11.0	−11:53:23	1.520	L	19.00	0.169	−26.49	E77
PKS 0349−14	03:51:28.6	−14:29:10	0.614	L	16.20	0.263	−26.74	N36
PKS 0402−362	04:03:53.8	−36:05:02	1.417	L	17.17	0.017	−28.13	E79
PKS 0403−132	04:05:34.0	−13:08:14	0.571	L	17.10	0.192	−25.64	N36
PKS 0405−123	04:07:48.5	−12:11:36	0.574	L	14.90	0.191	−27.85	N36
PKS 0414−06	04:17:16.7	−05:53:45	0.773	L	15.90	0.143	−27.72	N36
PKS 0420−014	04:23:15.8	−01:20:33	0.915	L	17.00	0.436	−27.14	N36
PKS 0440−00	04:42:38.6	−00:17:43	0.607	L	18.41	0.174	−24.49	N36
0624+6907	06:30:02.5	+69:05:04	0.370	Q	14.20	0.324	−27.36	L06, D08
PKS 0710+11	07:13:02.3	+11:46:15	0.768	L	16.60	0.488	−27.00	N36
MS0824.2+0327	08:26:52.9	+03:17:13	1.431	Q	20.20	0.132	−25.13	E78
MS08287+6614	08:33:17.9	+66:03:46	0.610	Q	18.00	0.131	−24.93	N36
PKS 0838+13	08:40:47.6	+13:12:23	0.684	L	18.10	0.309	−25.15	N35
US1867	08:53:34.2	+43:49:02	0.513	Q	16.40	0.112	−26.02	L06, D08
0903+169	09:06:31.9	+16:46:11	0.411	L	18.27	0.133	−23.56	L06, D08
TON392	09:12:17.8	+24:50:38	0.654	Q	16.00	0.148	−27.12	N36
MS09441+1333	09:46:52.0	+13:20:26	0.131	Q	16.05	0.132	−23.15	D08
0953+415	09:56:52.4	+41:15:22	0.234	Q	15.30	0.042	−25.17	D08
1001+291	10:04:02.5	+28:55:35	0.330	Q	15.50	0.072	−25.79	L06, D08
1004+130	10:07:26.1	+12:48:56	0.240	L	15.20	0.127	−25.35	D08
Z101733−0203	10:17:33.5	−02:03:07	1.343	Q	20.80	0.145	−24.37	E78
PKS 1015−31	10:18:09.3	−31:44:14	1.346	L	20.40	0.277	−24.77	E78
PKS 1018−42	10:20:03.9	−42:51:30	1.280	L	18.80	0.380	−26.26	E78
1058+110	11:00:47.8	+10:46:13	0.423	L	17.10	0.085	−24.80	D08
1100+772	11:04:13.7	+76:58:58	0.315	L	15.72	0.112	−25.43	D08
1116+215	11:19:27.6	+21:17:20	0.177	Q	14.70	0.075	−25.10	D08
1150+497	11:53:24.4	+49:31:09	0.334	L	17.10	0.071	−24.20	L06, D08
1202+281	12:04:42.1	+27:54:11	0.165	Q	15.60	0.070	−24.06	L06, D08
1208+322	12:10:37.6	+31:57:06	0.388	L	16.00	0.056	−25.64	D08
1216+069	12:19:20.9	+06:38:38	0.331	Q	15.65	0.072	−25.64	L06
MRK0205	12:21:44.0	+75:18:38	0.071	Q	15.24	0.139	−22.65	L06, D08
1222+125	12:25:12.9	+12:18:36	0.415	L	17.86	0.115	−23.98	D08
3C273	12:29:06.7	+02:03:08	0.158	L	12.90	0.068	−26.63	L06
1230+097	12:33:25.8	+09:31:23	0.415	Q	16.15	0.068	−25.69	L06, D08
Z124029−0010	12:40:29.7	−00:10:48	2.030	Q	19.80	0.074	−26.45	E78
PG1302−102	13:05:33.0	−10:33:19	0.286	L	15.20	0.141	−25.71	L06
1307+085	13:09:47.0	+08:19:49	0.155	Q	15.10	0.112	−24.43	L06, D08
1309+355	13:12:17.8	+35:15:21	0.184	L	15.64	0.040	−24.29	L06, D08

Table A1 – *continued*

Name	RA (J2000)	Dec. (J2000)	z	Radio loudness	m_V (mag)	A_V (mag)	M_V (mag)	References
(1)	(2)	(3)	(4)	(5)	(6)	(7)	(8)	(9)
Z133136−0002	13:31:36.2	−00:02:53	2.710	Q	20.70	0.084	−26.22	E78
1402+436	14:04:38.8	+43:27:07	0.320	Q	15.62	0.035	−25.60	D08
PG1416−129	14:19:05.7	−13:10:56	0.129	Q	16.10	0.311	−22.94	L06
1425+267	14:27:35.5	+26:32:14	0.366	L	15.68	0.062	−25.83	L06, D08
Z143220−0215	14:32:20.1	−02:15:47	2.476	Q	20.40	0.148	−26.35	E78
Z144022−0122	14:40:22.3	−01:22:33	2.244	Q	20.00	0.166	−26.51	E78
1444+407	14:46:45.9	+40:35:06	0.267	Q	15.70	0.046	−25.04	L06, D08
PKS J1511−10	15:13:44.9	−10:12:00	1.513	L	18.80	0.351	−26.68	E78
1512+37	15:14:43.0	+36:50:50	0.371	L	16.27	0.072	−25.30	L06, D08
PKS 1524−13	15:26:59.4	−13:51:01	1.687	L	20.50	0.400	−25.29	E78
3C323.1	15:47:43.5	+20:52:17	0.266	L	16.70	0.140	−24.04	L06, D08
1549+203	15:52:02.3	+20:14:02	0.250	Q	16.40	0.176	−24.25	D08
HS1623+7313	16:22:16.8	+73:06:15	0.621	Q	16.30	0.110	−26.68	N35
1635+119	16:37:46.5	+11:49:50	0.146	Q	16.50	0.171	−22.88	D08
3C345	16:42:58.8	+39:48:37	0.594	L	15.96	0.044	−26.89	L06, D08
3C351	17:04:41.4	+60:44:31	0.372	L	15.28	0.075	−26.29	L06, D08
1821+643	18:21:57.3	+64:20:36	0.297	Q	14.10	0.141	−26.89	L06, D08
3C422	20:47:10.4	−02:36:23	0.942	L	18.69	0.181	−25.54	N36
MC2112+172	21:14:56.7	+17:29:23	0.878	L	17.90	0.446	−26.12	N36
Q2125−4432	21:29:01.0	−44:19:50	2.503	Q	20.39	0.077	−26.38	E79
PKS 2128−12	21:31:35.3	−12:07:04	0.501	L	16.11	0.204	−26.26	L06
PKS 2135−14	21:37:45.2	−14:32:55	0.200	L	15.50	0.169	−24.65	L06
2141+175	21:43:35.5	+17:43:49	0.211	L	15.73	0.367	−24.53	L06, D08
Z215539−3026	21:55:39.7	−30:26:23	2.593	Q	20.44	0.085	−26.39	E79
2201+315	22:03:15.0	+31:45:38	0.295	L	15.58	0.410	−25.40	L06, D08
PKS 2204−20	22:07:33.9	−20:38:35	1.923	L	19.49	0.098	−26.63	E79
Z221139−3132	22:11:39.1	−31:32:53	2.391	Q	20.40	0.048	−26.28	E79
Z222702−3205	22:27:02.4	−32:05:36	2.177	Q	20.13	0.044	−26.29	E79
Q2225−403A	22:28:49.9	−40:08:34	2.410	Q	20.20	0.042	−26.50	E79
Q2225−403B	22:28:50.4	−40:08:27	0.932	Q	0.00	0.042	−44.20	E79
PKS 2227−08	22:29:40.1	−08:32:54	1.562	L	17.50	0.170	−28.06	E77
Z223048−2954	22:30:48.1	−29:54:05	2.652	Q	20.56	0.051	−26.32	E79
2247+140	22:50:25.3	+14:19:52	0.235	L	16.93	0.168	−23.54	D08
Z225950−3206	22:59:50.8	−32:06:03	2.225	Q	19.72	0.066	−26.77	E79
Z231751−3147	23:17:51.9	−31:47:40	2.628	Q	20.58	0.053	−26.28	E79
Z232755−3154	23:27:55.5	−31:54:36	2.737	Q	20.73	0.053	−26.20	E79
Z233451−2929	23:34:52.0	−29:29:20	2.669	Q	20.72	0.060	−26.17	E79
PKS 2345−167	23:48:02.6	−16:31:13	0.576	L	18.40	0.086	−24.35	N36
Q2348−4012	23:51:02.1	−39:56:18	1.500	Q	19.50	0.047	−25.96	E79

Note. (1) Quasar name; (2) and (3) quasar right ascension and declination in J2000; (4) catalogue redshift; (5) radio loudness (L = radio loud, Q = radio quiet); (6) catalogue apparent V-band magnitude; (7) Galactic V-band extinction; (8) absolute rest-frame V-band magnitude, as derived from the catalogue apparent V-band magnitude, k-corrected assuming the Francis et al. (1991) template; (9) data sources: L06; D08; E*xx* = new ESO/3.6 m observations (E77 = September, 2006; E78 = March, 2007; E79 = September, 2007); N*xx* = new NOT observations (N35 = April, 2007; N36 = October, 2007).

Table A2. Journal of the new observations.

Name	z	Run	Obs. date (yy/mm/dd)	Seeing (arcsec)	S/N	δZP (mag)
(1)	(2)	(3)	(4)	(5)	(6)	(7)
PKS 0000−177	1.465	E77	05/09/30	1.9	17.8	0.02
Q0040−3731	1.780	E77	05/09/30	2.0	19.5	0.02
SGP2:36	1.756	E79	07/09/10	1.2	13.3	0.11
SGP5:46	0.955	E79	07/09/10	1.5	26.1	0.06
SGP4:39	1.716	E79	07/09/11	1.4	38.4	0.05
PKS 0100−270	1.597	E77	05/09/30	1.7	17.5	0.02
PKS 0113−283	2.555	E79	07/09/11	1.5	26.2	0.09
0119−370	1.320	E79	07/09/11	1.4	31.7	0.11
0152−4055	1.650	E79	07/09/12	1.5	20.7	0.04
PKS 0155−495	1.298	E77	05/09/30	1.8	33.9	0.02
PKS 0159−11	0.669	N36	07/10/17	0.7	63.4	0.07
PB6708	0.868	N36	07/10/17	0.8	34.7	0.07
KUV03086−0447	0.755	N36	07/10/19	1.5	24.0	0.03
MZZ01558	1.829	E79	07/09/12	2.0	26.9	0.12
US3828	0.515	N36	07/10/18	0.7	9.1	0.02
Q0335−3546	1.841	E79	07/09/09	1.0	25.2	0.10
PKS 0348−120	1.520	E77	05/09/30	1.7	103.7	0.02
PKS 0349−14	0.614	N36	07/10/17	0.8	6.0	0.07
PKS 0402−362	1.417	E79	07/09/09	1.0	97.3	0.15
PKS 0403−132	0.571	N36	07/10/19	1.3	17.5	0.03
PKS 0405−123	0.574	N36	07/10/17	0.8	21.7	0.07
PKS 0414−06	0.773	N36	07/10/17	0.6	15.4	0.07
PKS 0420−014	0.915	N36	07/10/19	1.1	10.5	0.01
PKS 0440−00	0.844	N36	07/10/18	0.7	30.8	0.00
PKS 0710+11	0.768	N36	07/10/19	1.1	70.6	0.03
MS0824.2+0327	1.431	E78	07/03/23	1.0	13.4	0.05
MS08287+6614	0.610	N36	07/10/18	0.9	33.7	0.02
PKS 0838+13	0.684	N35	07/04/09	0.8	54.7	0.00
TON392	0.654	N36	07/10/17	0.7	57.2	0.07
Z101733−0203	1.343	E78	07/03/23	0.9	79.1	0.05
PKS 1015−31	1.346	E78	07/03/25	1.0	26.2	0.05
PKS 1018−42	1.280	E78	07/03/25	1.0	11.4	0.05
PKS 1102−242	1.666	E78	07/03/24	0.8	18.4	0.05
Z124029−0010	2.030	E78	07/03/23	1.1	20.3	0.05
Z133136−0002	2.710	E78	07/03/25	1.1	16.1	0.05
Z143220−0215	2.476	E78	07/03/24	1.0	14.0	0.05
Z144022−0122	2.244	E78	07/03/25	0.9	49.8	0.05
PKS J1511−10	1.513	E78	07/03/23	1.3	19.7	0.05
PKS 1524−13	1.687	E78	07/03/24	0.7	10.3	0.05
HS1623+7313	0.621	N35	07/04/09	1.5	5.7	0.00
3C422	0.942	N36	07/10/18	1.0	72.3	0.02
MC2112+172	0.878	N36	07/10/19	1.0	49.5	0.03
Q2125−4432	2.503	E79	07/09/09	1.3	14.4	0.08
Z215539−3026	2.593	E79	07/09/11	1.9	11.3	0.05
PKS 2204−20	1.923	E79	07/09/10	1.6	24.6	0.06
4C02.54	0.976	N36	07/10/18	0.9	16.0	0.02
Z221139−3132	2.391	E79	07/09/10	1.2	11.6	0.06
Z222702−3205	2.177	E79	07/09/08	2.3	19.6	0.00
Q2225−403A	2.410	E79	07/09/09	1.3	76.0	0.07
Q2225−403B	0.932	E79	07/09/09	1.3	20.2	0.07
PKS 2227−08	1.562	E77	05/09/30	2.2	32.8	0.00
Z223048−2954	2.652	E79	07/09/10	1.0	18.5	0.06
Z225950−3206	2.225	E79	07/09/08	2.4	34.1	0.08
Z231751−3147	2.628	E79	07/09/12	1.8	27.5	0.14
Z232755−3154	2.737	E79	07/09/09	1.3	13.7	0.07
Z233451−2929	2.669	E79	07/09/11	1.3	54.0	0.09
PKS 2345−167	0.576	N36	07/10/19	1.2	12.2	0.03
Q2348−4012	1.500	E79	07/09/11	1.3	42.6	0.01
ZC2351+010B	0.810	N36	07/10/19	1.3	7.9	0.03

Note. (1) Quasar name; (2) catalogue redshift; (3) run of observation (see Table 1 for the description of each run); (4) date of observations; (5) seeing, computed from the profiles of field stars in corollary images; (6) spectral S/N (per pixel); (7) uncertainty in the photometric calibration (in magnitudes).

Table A3. Continuum and line fit parameters.

Name	z	α	log F_λ (erg s^{-1} cm^{-2} Å^{-1})	log λL_λ (erg s^{-1})	Line	FWHM (km s^{-1})	log $\mathcal{M}_{BH}$ ($M_\odot$)	log L/L_{Edd}
(1)	(2)	(3)	(4)	(5)	(6)	(7)	(8)	(9)
PKS 0000−177	1.465	−1.05	−15.67	45.94	Mg II	6857	9.71	−1.16
Q0040−3731	1.780	−0.92	−14.93	46.55	C IV	2561	9.16	−0.13
SGP2:36	1.756	−1.52	−16.42	45.03	C IV	6123	9.13	−1.62
SGP5:46	0.955	−0.74	−16.13	45.02	Mg II	3873	8.77	−1.14
0054+144	0.171	−1.38	−15.84	43.82	Hβ	8220	8.73	−2.04
SGP4:39	1.716	−1.33	−16.16	45.27	C IV	1852	8.12	−0.37
PKS 0100−270	1.597	−1.57	−15.24	46.46	Mg II	3539	9.37	−0.30
LBQS0100+0205	0.393	−1.48	−14.69	45.20	C IV	3966	8.85	−1.17
0110+297	0.363	−2.36	−15.57	44.81	Hβ	6149	9.13	−1.45
PKS 0113−283	2.555	−1.10	−15.36	46.50	C IV	8014	10.18	−1.20
0119−370	1.320	−1.01	−16.22	45.29	Mg II	10178	9.74	−1.84
0133+207	0.425	−1.63	−14.68	45.27	C IV	4478	9.00	−1.25
		−2.37	−15.57	44.96	Hβ	8845	9.55	−1.72
3C48	0.367	−1.80	−14.83	45.55	Hβ	4011	9.24	−0.82
HB890137+012	0.260	−0.90	−14.99	44.49	C IV	6778	8.93	−1.96
0152−4055	1.650	−0.91	−15.91	45.83	Mg II	4664	9.32	−0.86
PKS 0155−495	1.298	−1.71	−15.92	45.56	Mg II	4511	9.16	−0.99
PKS 0159−11	0.669	−1.88	−14.58	46.19	Mg II	3703	9.29	−0.49
B0204+2916	0.109	−0.81	−14.81	44.40	Hβ	8964	9.18	−1.91
0244+194	0.176	−2.78	−14.77	44.90	Hβ	4675	8.94	−1.17
KUV03086−0447	0.755	−0.99	−14.84	46.06	Mg II	2771	8.97	−0.30
MZZ01558	1.829	−0.66	−16.19	45.31	C IV	8012	9.53	−1.74
US3828	0.515	−4.07	−14.82	45.68	Mg II	4066	9.13	−0.84
Q0335−3546	1.841	−1.43	−15.76	45.75	C IV	3452	9.01	−0.78
PKS 0348−120	1.520	−1.80	−15.72	45.93	Mg II	5044	9.43	−0.89
PKS 0349−14	0.614	−1.50	−14.36	46.32	Mg II	8442	10.07	−1.14
PKS 0402−362	1.417	−0.83	−15.17	46.41	Mg II	4251	9.50	−0.48
PKS 0403−132	0.571	−2.53	−14.96	45.65	Mg II	3709	9.04	−0.78
PKS 0405−123	0.574	−1.72	−13.83	46.79	Mg II	6572	10.07	−0.67
PKS 0414−06	0.773	1.24	−14.75	46.18	Mg II	12790	10.36	−1.57
PKS 0420−014	0.915	−0.36	−14.97	46.13	Mg II	3601	9.24	−0.50
PKS 0440−00	0.607	−0.83	−15.17	45.50	Mg II	5129	9.25	−1.14
0624+6907	0.370	−1.08	−13.45	46.38	C IV	3583	9.42	−0.56
		−3.04	−14.28	46.12	Hβ	3631	9.53	−0.54
PKS 0710+11	0.768	−2.92	−14.74	46.18	Mg II	8339	9.99	−1.20
MS0824.2+0327	1.431	−1.57	−15.82	45.76	Mg II	2748	8.81	−0.44
MS08287+6614	0.610	−0.74	−15.19	45.49	Mg II	5773	9.35	−1.25
PKS 0838+13	0.684	−0.37	−16.02	44.78	Mg II	3840	8.66	−1.27
US1867	0.513	−1.03	−14.38	45.77	C IV	4222	9.22	−0.97
		−2.08	−15.29	45.44	Hβ	2279	8.69	−0.38
0903+169	0.411	−1.29	−14.97	44.96	C IV	4989	8.92	−1.48
TON392	0.654	−1.23	−14.46	46.29	Mg II	4905	9.58	−0.68
MS09441+1333	0.131	−1.84	−14.83	44.59	Hβ	3230	8.40	−0.94
0953+415	0.234	−3.07	−14.32	45.63	Hβ	3606	9.19	−0.69
1001+291	0.330	−2.38	−15.11	45.18	Hβ	1977	8.33	−0.28
		−1.21	−13.85	45.86	C IV	3072	9.00	−0.66
1004+130	0.240	−1.99	−14.67	45.32	Hβ	6010	9.45	−1.26
Z101733−0203	1.343	−1.12	−16.90	44.61	Mg II	3219	8.41	−1.19
PKS 1015−31	1.346	1.50	−16.02	45.50	Mg II	5112	9.24	−1.13
PKS 1018−42	1.280	−0.64	−15.38	46.09	Mg II	4353	9.37	−0.67
1058+110	0.423	−2.03	−15.88	44.65	Hβ	7460	9.20	−1.68
1100+772	0.315	−2.46	−14.38	45.86	Hβ	6980	9.94	−1.21
1116+215	0.177	−2.39	−14.05	45.62	Hβ	2671	8.90	−0.41
1150+497	0.334	−1.49	−14.41	45.30	C IV	3966	8.91	−1.13
		−1.86	−15.61	44.69	Hβ	3868	8.65	−1.09
1202+281	0.165	−1.00	−14.54	44.49	C IV	2560	8.09	−1.12
		−2.38	−14.97	44.64	Hβ	5186	8.86	−1.35
1208+322	0.388	−2.06	−15.23	45.20	Hβ	5279	9.26	−1.19
1216+069	0.331	−1.33	−13.86	45.86	C IV	2560	8.84	−0.50
MRK0205	0.071	−1.32	−13.56	44.76	C IV	2944	8.36	−1.12
		−1.19	−14.29	44.61	Hβ	3277	8.45	−0.97
1222+125	0.415	−2.05	−15.56	44.94	Hβ	7529	9.40	−1.59
3C273	0.158	−1.25	−12.89	46.09	C IV	3199	9.16	−0.59

Table A3 – *continued*

Name	z	α	log F_λ (erg s^{-1} cm^{-2} Å^{-1})	log λL_λ (erg s^{-1})	Line	FWHM (km s^{-1})	log $\mathcal{M}_{\rm BH}$ ($M_\odot$)	log $L/L_{\rm Edd}$
(1)	(2)	(3)	(4)	(5)	(6)	(7)	(8)	(9)
1230+097	0.415	1.38	−14.21	45.73	C IV	3327	8.99	−0.78
		−2.17	−15.21	45.30	Hβ	4765	9.24	−1.07
Z124029−0010	2.030	−0.87	−15.74	45.87	C IV	6529	9.65	−1.30
PG1302−102	0.286	−0.96	−13.35	46.21	C IV	3966	9.41	−0.72
1307+085	0.155	−1.71	−14.20	45.35	Hβ	3494	9.00	−0.78
		−0.95	−13.90	45.07	C IV	3327	8.63	−1.08
1309+355	0.184	−1.12	−13.84	45.30	C IV	3199	8.73	−0.95
		−2.21	−15.07	44.64	Hβ	4434	8.72	−1.21
Z133136−0002	2.710	−0.68	−16.08	45.84	C IV	6027	9.57	−1.25
1402+436	0.320	−1.14	−15.74	44.52	Hβ	2763	8.25	−0.86
PG1416−129	0.129	−1.78	−14.18	44.60	C IV	3838	8.50	−1.42
1425+267	0.366	−1.24	−14.27	45.54	C IV	8057	9.66	−1.64
		−2.80	−15.17	45.21	Hβ	8090	9.64	−1.56
Z143220−0215	2.476	−1.41	−16.15	45.67	C IV	5729	9.43	−1.28
Z144022−0122	2.244	−1.01	−15.95	45.77	C IV	6225	9.55	−1.30
1444+407	0.267	−2.26	−15.95	44.11	Hβ	2694	7.96	−0.98
		−1.40	−13.74	45.74	C IV	5117	9.38	−1.16
PKS J1511−10	1.513	−1.56	−15.71	45.93	Mg II	4662	9.36	−0.82
1512+37	0.371	−1.86	−14.00	45.82	C IV	3966	9.20	−0.90
		−1.96	−15.30	45.10	Hβ	8910	9.65	−1.68
PKS 1524−13	1.687	−2.05	−15.28	46.13	C IV	4778	9.52	−0.91
1549+203	0.250	−2.28	−15.14	44.88	Hβ	1880	8.06	−0.31
3C323.1	0.266	−2.05	−15.47	44.60	Hβ	4734	8.76	−1.29
		−1.39	−14.09	45.40	C IV	4222	9.02	−1.14
HS1623+7313	0.621	−1.50	−15.41	45.29	Mg II	3783	8.88	−0.98
1635+119	0.146	−1.38	−15.04	44.46	Hβ	5704	8.83	−1.50
3C345	0.594	−0.84	−15.73	45.15	Hβ	3938	8.98	−0.96
		−0.78	−14.32	45.98	C IV	4350	9.37	−0.91
3C351	0.372	−1.18	−13.88	45.95	C IV	5117	9.49	−1.06
		−1.69	−15.71	44.69	Hβ	9256	9.41	−1.85
1821+643	0.297	−2.44	−14.02	46.15	Hβ	5250	9.88	−0.86
		−1.24	−13.29	46.30	C IV	3966	9.46	−0.68
3C422	0.942	5.16	−15.40	45.74	Mg II	1594	8.34	0.01
MC2112+172	0.878	−1.76	−15.94	45.12	Mg II	2648	8.49	−0.76
Q2125−4432	2.503	−1.04	−16.15	45.68	C IV	6704	9.57	−1.41
PKS 2128−12	0.501	−1.03	−13.87	46.26	C IV	4733	9.59	−0.85
PKS 2135−14	0.200	−0.59	−14.14	45.09	C IV	4861	8.98	−1.41
2141+175	0.211	−2.28	−14.72	45.14	Hβ	5179	9.19	−1.18
		−0.68	−14.00	45.28	C IV	4222	8.96	−1.20
Z215539−3026	2.593	−1.35	−15.97	45.90	C IV	5065	9.45	−1.07
2201+315	0.295	−1.60	−13.37	46.22	C IV	4733	9.57	−0.87
		−2.77	−14.58	45.59	Hβ	3022	9.01	−0.55
PKS 2204−20	1.923	−0.97	−16.22	45.34	C IV	3348	8.76	−0.94
Z221139−3132	2.391	−0.93	−16.12	45.66	C IV	3756	9.05	−0.91
Z222702−3205	2.177	−1.41	−16.11	45.58	C IV	6573	9.50	−1.44
Q2225−403A	2.410	−1.03	−15.70	46.09	C IV	5372	9.60	−1.03
Q2225−403B	0.932	−0.88	−16.13	44.99	Mg II	4571	8.90	−1.30
PKS 2227−08	1.562	0.00	0.00	46.91	Mg II	1755	8.94	0.58
Z223048−2954	2.652	−1.12	−16.22	45.68	C IV	5450	9.39	−1.23
2247+140	0.235	−1.48	−15.27	44.68	Hβ	3178	8.48	−0.93
Z225950−3206	2.225	−1.24	−15.78	45.92	C IV	8110	9.87	−1.47
Z231751−3147	2.628	−1.36	−16.34	45.54	C IV	2364	8.56	−0.54
Z232755−3154	2.737	−0.95	−16.34	45.59	C IV	3009	8.81	−0.74
Z233451−2929	2.669	−1.18	−16.31	45.59	C IV	2676	8.70	−0.63
PKS 2345−167	0.576	−0.23	−15.05	45.57	Mg II	3350	8.91	−0.73
Q2348−4012	1.500	−1.23	−15.82	45.82	Mg II	3223	8.98	−0.55

Note. (1) Quasar name; (2) catalogue redshift; (3) spectral index of the fitted power law defined so that log $F_\lambda = \alpha \log \lambda +$ constant; (4) quasar monochromatic flux as estimated from the fitted power law at $\lambda = 5100$, 3000 and 1350 Å (for Hβ, Mg II and C IV, respectively); (5) monochromatic luminosity as computed from column (4) and assuming $H_0 = 70$ km s^{-1} Mpc^{-1}, $\Omega_{\rm m} = 0.3$, $\Omega_\Lambda = 0.7$; (6) fitted line; (7) FWHM, estimated with GH fit after modelling Fe II emission; (8) BH masses, assuming f(Hβ, Mg II) = 1.6 and f(C IV) = 2.4. (9) Eddington ratio, assuming $L_{\rm Bol}/\lambda L_\lambda = 9.26$, 5.15 and 3.81 for H$\beta$, Mg II and C IV, respectively.

This paper has been typeset from a TEX/LATEX file prepared by the author.